Applied Surface Science 589 (2022) 152965

Contents lists available at ScienceDirect

Applied Surface Science

journal homepage: www.elsevier.com/locate/apsusc

Full Length Article

Deepening of nanograting structures on Si by a two-step laser spatial-selective amorphization strategy combined with chemical etching

Xiuyun Li [a,b], Ruiyan Li [a,b], Zhi Yu [a,b,e,*], Jun Xing [c], Wenchi Kong [a,b], Yue Wang [d], Jianjun Yang [a,b,*]

[a] GPL, State Key Laboratory for Applied Optics, Changchun Institute of Optics, Fine Mechanics and Physics, Chinese Academy of Sciences, Changchun 130033, China
[b] University of Chinese Academy of Sciences, Beijing 100049, China
[c] Xinjiang Key Laboratory of Solid State Physics and Devices, School of Physics and Technology, Xinjiang University, 666 Shengli Road, Urumqi 830046, China
[d] Department of Chemistry, College of Sciences, Northeastern University, Shenyang 110819, China
[e] The Key Laboratory of Bionic Engineering (Ministry of Education), Jilin University, Changchun 130012, China

ARTICLE INFO

Keywords:
Two-step spatial-selective amorphization
LFE-LIPSSs
Enhanced antireflection
SERS polarization dependence effect

ABSTRACT

Femtosecond laser induced periodic surface structures (LIPSSs) have been implemented on various materials. However, its further development in manipulation of optical properties is hindered by the shallow depth. Herein, the paper proposes a novel method of two-step spatial-selective amorphization for producing the deep regular nanogratings on silicon by femtosecond laser and chemical etching with HF acid. In the first step, the spatially periodic amorphization of silicon surface is fabricated by the surface plasmon excitation of the incident femtosecond laser, the chemical etching of which produces the shallow gratings with a period of 765 nm, or so-called prefabricated-LIPSSs (pre-LIPSSs). During the second step, the spatial-selective amorphization of sample takes place by exploiting the local field enhancement of laser irradiation within the grooves. After chemical etching, the deep local field enhancement assisted LIPSSs (LFE-LIPSSs) are formed, with a three-fold larger depth of 155 nm but an invariable period. Comparing with the pre-LIPSSs, the LFE-LIPSSs show 45% increase in antireflection performance at around 700 nm and surface-enhanced Raman scattering (SERS) anisotropy ratio is increased about four times with 4-MBA molecules as probe molecules. This work provides a promising approach to fabricate deeper LIPSSs for more effectively controlling the optical properties of materials by femtosecond laser.

1. Introduction

In the information era, the high performance of optical and electronic devices plays an irreplaceable role in developing science and technology, and micro/nano-structure materials are critical points in their development. Especially for the optical devices, micro/nano-structures have drawn considerable research interests, due to their excellent performance in modifying optical characteristics of the material surface, including promoted absorptivity, [1,2] enhanced luminescence, [3] and light field regulation [4]. Researchers can endow micro/nano-devices with different functions and manipulate the light acting on the material's surface by the design of appropriate micro/nano-structures, which broadens its application in various fields, such as solar-thermal devices, [5,6] surface-enhanced Raman scattering (SERS), [7–9] integration optical devices, [10] metamaterials, [11,12] and nonlinear optics [13]. Thus, the advanced micro/nano-manufacturing techniques are essential for promoting the development of such devices. To date, the existing strategies for the micro/nano-fabrication, including electron beam lithography, [14] focused ion beam milling, [15] and photolithography, [16] have been widely used with the high resolution and precision. However, there are still some restrictions on these techniques, such as the expensive equipment, extremely complicated processes, lack of flexibility, and mask preparation.

During the past few years, we have witnessed a tremendous surge of interest in the study of ultrafast lasers which are becoming more user-friendly and less expensive every year. The technique of femtosecond laser processing with the high spatial resolution and minimal thermal damage provides a new idea for the mirco/nanoscale fabrication [17].

* Corresponding authors at: GPL, State Key Laboratory for Applied Optics, Changchun Institute of Optics, Fine Mechanics and Physics, Chinese Academy of Sciences, Changchun 130033, China.
E-mail addresses: zhiyu@ciomp.ac.cn (Z. Yu), jjyang@ciomp.ac.cn (J. Yang).

https://doi.org/10.1016/j.apsusc.2022.152965
Received 12 November 2021; Received in revised form 13 February 2022; Accepted 27 February 2022
Available online 5 March 2022
0169-4332/© 2022 Elsevier B.V. All rights reserved.

Even though its resolution and precision cannot match with the traditional techniques, the unique advantages of high efficiency, convenience, low cost, and flexible 3D machining can be given in the material fabrication. Traditional manufacturing techniques can't fabricate structures directly inside silicon, but Tokel et al. successfully fabricated complex 3D microstructures deep inside silicon by ultrafast laser with chemical etching [18]. Especially, the intriguing physical mechanisms of femtosecond laser-material interaction provide a distinctive perspective for manipulating physical and chemical properties of the material surface [19].

With the development of LIPSSs, which is firstly discovered on a germanium surface in 1965 by Birnbaum, the utilization of femtosecond laser irradiation for this purpose has made tremendous progresses especially in the structure dimension and accuracy [20,21]. More importantly, femtosecond-LIPSSs on multifarious materials, including metals, [22,23] semiconductors [24–26] and insulators, [27–29] can exhibit multiple functional features. The preparation of periodic structures on the surface of tungsten by Qiao et al. significantly improved the absorption efficiency [30]. By taking advantage of the flexible machining of the femtosecond laser, Bai et al. fabricated Cu-Ag LIPSSs in the microchannel for sensitive SERS detection [31]. By focusing the femtosecond laser on graphene oxide (GO) films, Zou et al. successfully obtained the reduced-GO-LIPSSs films to cause the enhanced light absorption and an anisotropic photoresponse [32]. Owing to the excellent properties, silicon has been widely studied for the development of the regular LIPSSs. Recently, Zhang et al. presented a pulse shaping system to fabricate homogeneous LIPSSs on Si surface [33]. In particular, Siegel et al. have demonstrated to fabricate the crystalline-amorphous LIPSSs on silicon by controlling the laser power [34–36]. Furthermore, several reports have combined laser processing silicon crystalline-amorphous LIPSSs with chemical etching, which can control the diffraction efficiency on Si surface by tuning the structure heights [26,37,38]. As it is known, both the deep and regular distributions of LIPSSs are beneficial for promoting optical characterizations, including antireflection and diffraction efficiency. However, the obtaining of femtosecond-LIPSSs with deeper and more regular profiles is still a challenge.

In this paper, we proposed a novel strategy by two-step spatial-selective amorphization for fabricating deep nanograting structures on a Si surface using a femtosecond laser with chemical etching. Herein, due to the interference of weak surface plasmon polaritons (SPP) and incident laser, the regular crystalline/amorphous periodically staggered gratings perpendicular to the polarization direction of femtosecond laser were first created on the Si surface, followed by the etching process to acquire the prefabricated-LIPSSs (pre-LIPSSs). In the second step, the obtained local field enhancement assisted LIPSSs (LFE-LIPSSs), without change in the spatial period of the structures, can be further deepen because the enhanced light field in grooves played a dominate role. After HF etching, the maximum depth of the LFE-LIPSSs (155 nm) can be increased to three times comparing to that of pre-LIPSSs (50 nm), coupled with the improved antireflection and enhanced polarization dependence SERS performance. To a certain extent, this study improved the controllability and optical performance of LIPSSs and provided a novel approach in promoting femtosecond laser processing techniques.

2. Experimental section

2.1. Materials

The single-face polished crystalline silicon wafers (1 0 0) were purchased from Sibranch Electronic Science and Technology Company. Hydrofluoric acid and ethanol were purchased from Beijing Chemical Works. 4-Mercaptobenzoic acid (4-MBA) was bought from Sigma-Aldrich. Deionized water (18.0 MΩ cm^{-1}) was used during the experiment.

2.2. Fabrication of periodic structures

A Ti: sapphire chirped-pulse amplification femtosecond laser system (Spitfire Ace, Spectra Physics, USA) was used for the structure fabrication, which delivers the pulse trains with a time duration of $\tau = 35$ fs and a central wavelength of $\lambda = 800$ nm at a repetition rate of 1 kHz. As shown in Figure S1, a combination of a half-wave plate and a Glan prism was used to change the linear polarization and the laser pulse energy. A cylindrical lens (focal length = 50 mm) was adopted for focusing the femtosecond laser beam into a narrow line-shaped spot with a width of 6.08 μm and a length of 8.5 mm, respectively.

2.3. Preparation of samples for SERS measurements

First, the sample surfaces were coated with 20-nm-thick Au or Ag film by thermal evaporation approach, and then they were immersed into 10^{-3} M 4-MBA solution at room temperature for two hours. After that, the samples were taken out to be flushed with ethanol and dried by N_2 flow for SERS measurements.

2.4. Characterization

The scanning electron microscope (SEM) images were obtained from a Hitachi S-4800. The detailed morphology of structures was measured by an atomic force microscope (AFM) (Bruker, Billerica, MA, USA). The metal films were deposited by the thermal vapor deposition coating machine (ZHD-400, Beijing Technol Science CO., LTD). The Raman spectra were collected by a LabRAM HR Evolution Raman spectrometer (Horiba Jobin Yvon) with three excitation laser wavelengths ($\lambda = 473$ nm, 532 nm and 785 nm). The reflection spectra were measured by an ARM spectrometer purchased from Shanghai Ideaoptics Company, which is integrated with a microscopic system. In the experiment, the normal incident light was focused by an objective lens (NA = 0.9) to generate a cone-shaped beam with an angle range of 120° as the light source, and the reflective spectra were collected from normal direction of sample surface.

3. Results and discussion

The LFE-LIPSSs were carried out with the processing steps shown in Fig. 1. At first, the crystalline-amorphous periodic structures were developed on a silicon surface under femtosecond laser irradiation, followed by the smoothing and deepening step with a 5% HF solution. Afterwards, the obtained LIPSSs undergo the aforementioned processes once again with the appropriate laser parameters.

3.1. Fabrication of shallow LIPSSs by the SPP based amorphization on silicon surface

As previously reported, the formation of LIPSSs with a low spatial frequency is extensively attributed to interference of the incident laser and the excitation of SPP [39–41]. In our cases, when the crystalline silicon was irradiated by the focal intensive femtosecond laser, its surface is ready to exhibit metal-like properties to promote the SPP excitation. The subsequent laser-SPP interference would likely result in the periodic energy fringes. For the surface local areas with the strong laser energy distribution, silicon material is primed to have a transition from the crystalline to the amorphous phase, whereas there is almost no change for the surface local areas with the low laser energy distribution [26,37]. As a result, the crystalline and amorphous phases were alternately arranged on silicon surfaces with a spatial period of $\Lambda = 765$ nm. Figure S2A shows a SEM image of the achieved periodic structures, which exhibits the uniform grating profiles with orientation perpendicular to the laser polarization direction. However, because of the laser ablation happening during this process, the surface roughness of the structures is seen evidently. Thus, the following procedure of smoothing

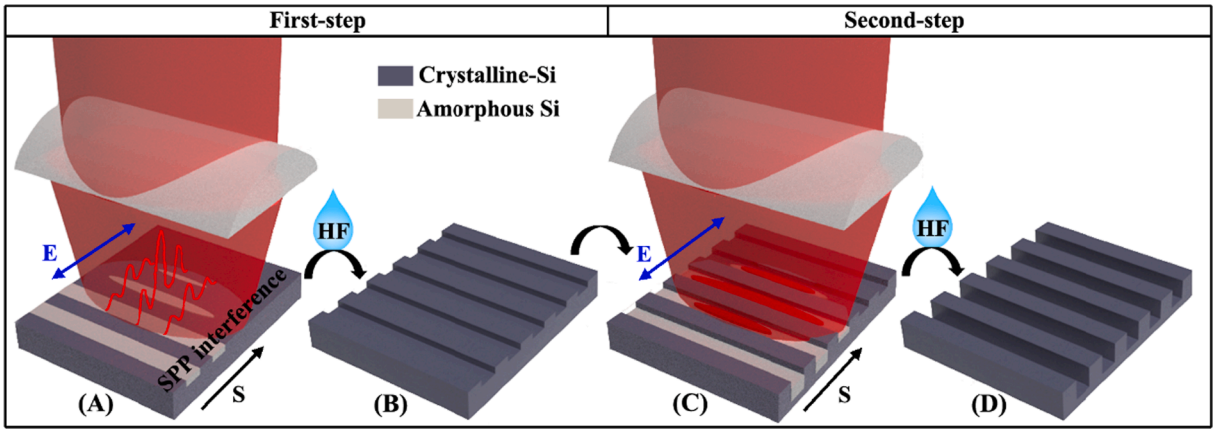

Fig. 1. Schematic illustration of the procedures for fabricating the deep LIPSSs. (A) Initial crystalline-amorphous LIPSSs were fabricated on the silicon wafer by the femtosecond laser irradiation. (B) Geometric profiles of LIPSSs after 5% HF etching. (C) The fabrication of LIPSSs by the localized light field enhancement. (D) Geometric profiles of LFE-LIPSSs after 5% HF etching.

and deepening is carried out by chemical etching with HF solution to remove the amorphiziaton areas [42,43]. Because the etching rate of amorphous silicon in the HF solution is much higher than that of crystalline silicon, the regions of unmodified crystalline silicon can serve as a mask, and the amorphous regions are rapidly etched to result in the smoother and deeper grating structures, as shown in Figure S2B.

During the first-step amorphous process, the structure formation, including the morphology and the arrangement, is seriously affected by the laser parameters. A detailed exploration of this behavior is shown in Figure S3. Because the excited SPP intensity increases with the higher energy fluence and spatial overlapping of the laser spot, the regular arrangement of the grating structures can be obtained under certain conditions, while either the excessive or the insufficient ablation of the material exist beyond the optimal conditions. The resultant nanostructure formation vs. the laser parameters are summarized in Fig. 2, which can be divided into four parts. Namely, at the conditions (I region) of both the lower laser fluence and the higher scanning speed, the morphology of the silicon surface has no apparent change. With gradually increasing the laser fluence and decreasing the scanning speed, the regular distribution of the crystalline-amorphous LIPSSs is produced (II region). It is extensively accepted that interference of the weak SPP excitation and the incident laser can make the Si surface melt and recrystallize rapidly, transforming crystalline silicon into an amorphous phase [34–36]. Thus, the spatial periodically arranged crystalline-amorphous silicon gratings are finally formed. Clearly, the regular LIPSSs will be destroyed by the strong material ablation when both the energy fluence and the number of pulses overlapping increase continuously, resulting in the irregular LIPSSs decorated with 2D nanohole chains (III region). With further altering the laser parameters, the stronger SPP is excited and the irregular ablative structures would like to

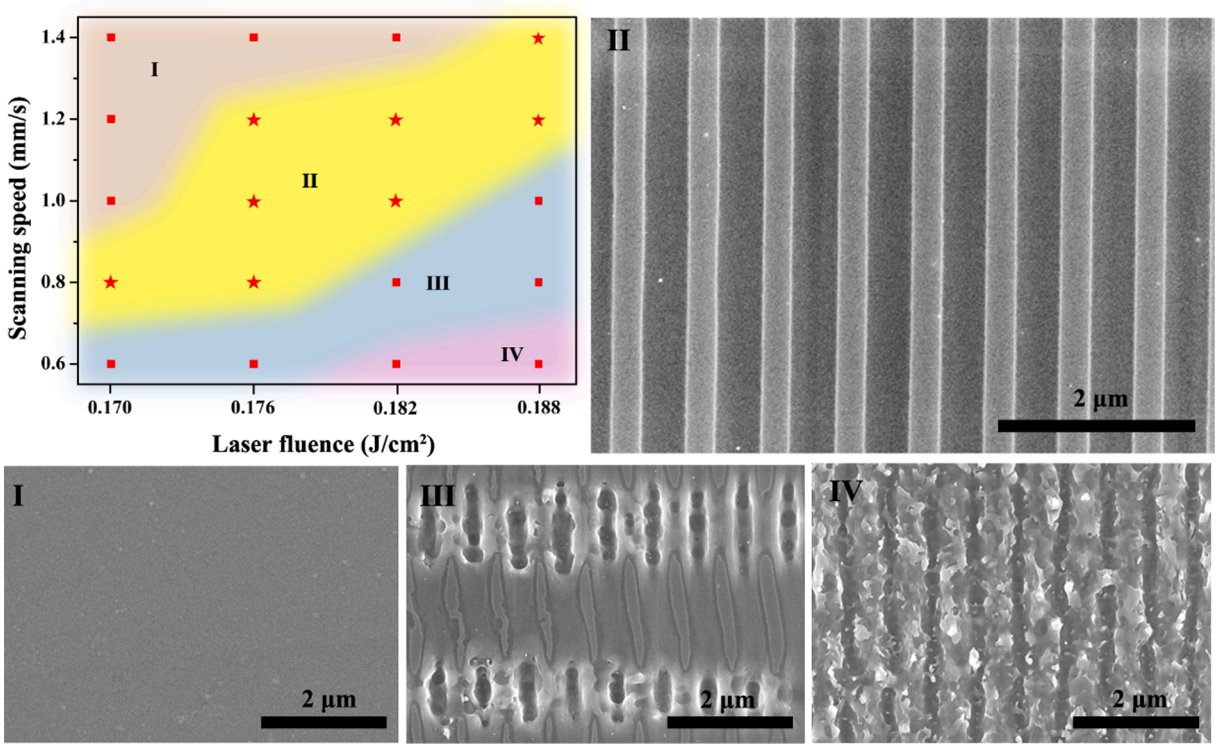

Fig. 2. Dynamic ranges for the structures formation on silicon surface with different femtosecond laser parameters. (I) None structure formation, (II) regular LIPSSs, (III) irregular LIPSSs decorated with nanohole chains, and (IV) strong ablative LIPSSs.

generate on the surface (IV region). Taking into account of the homogenous light field induced by the structures, the uniform structures formed under the conditions of $F = 0.176$ J cm^{-2} and $v = 1$ mm s^{-1} are selected for our further experiment. In addition, we also explored the effect of etching time on the surface morphology of the nanostructures, as shown in Figure S4 and S5. The detailed analysis is illustrated in the supporting information, which indicates that the optimal etching time of 40 min can cause the depth of the pre-LIPSSs up to 50 nm.

3.2. Fabrication of deep LIPSSs by the locally enhanced laser field amorphization process

Although HF etching can optimize the quality and depth of LIPSSs, the degree of the surface morphology change is still restricted by some reasons such as the limited thickness of amorphous silicon, thus, limiting the optical characteristics of the nanostructures. Based on that, we put forward a secondary spatial-selective amorphization strategy to increase the depth of the nanograting structures without changing period through the local field enhancement of femtosecond laser irradiation caused by the pre-LIPSSs. Herein, the Si slice with the shallow pre-LIPSSs is further irradiated by the femtosecond laser with appropriate parameters followed by HF etching process for 40 min to optimize the structural accuracy. During the secondary laser irradiation, the adopted scanning direction and laser polarization are same as the first step. Fig. 3 shows the corresponding SEM images of the structure formation under the four stages of processing, illustrating the structural changes in both the shape and the depth during each procedure. The modulation of LFE-LIPSSs approximates 155 nm in depth, about three times than that of the pre-LIPSSs, but structures still maintain both the spatial period of $\Lambda =$ 765 nm and the high uniform distribution.

To elucidate the formation mechanism of the deep LFE-LIPSSs, we employ the finite-difference time-domain (FDTD) method to simulate the electric field distribution of the incident femtosecond laser on the pre-fabricated LIPSSs, where a 3D model is used for simulating the E-field distribution of structure surface excited by $\lambda = 800$ nm light. The geometric design of the pre-LIPSSs, with a spatial period of $\Lambda = 765$ nm and a modulation depth of 50 nm, respectively, is consistent with the experiment observations. The simulation results (Fig. 4) display that the electric field intensities among the grooves (b) can be up to 2.25 times stronger than those on ridges (a), which is originated from the following facts: when the femtosecond laser irradiates the pre-LIPSSs on the silicon surface, the cavity modes of the grooves are excited to generate the strong local field enhancement at the antinode position [44]. As a result, the electric field on the surface is redistributed, and the more energy will be localized inside the grooves. Thus, with irradiation of appropriate laser parameters, the enhanced light field within the grooves can further cause the secondary amorphization within the grooves, while the lower electric field intensity on the structures is too weak to induce a phase change. As a result, after the amorphous Si is removed by HF etching, the modulation depth of the LIPSSs tends to increase significantly.

As a matter of fact, the formation of the regular deep LFE-LIPSSs is critically sensitive to the femtosecond laser parameters, which is also explored in the experiment. Figure S6 and Fig. 5A-D display the SEM images and AFM micrographs for the achieved diverse nanograting structures at a constant scanning speed ($v = 1$ mm s^{-1}) and etching time ($t = 40$ min) while the laser fluence is varied from $F = 0.099$ to 0.205 J cm^{-2}, which reveals the formation of the regular deep LFE-LIPSSs at the suitable fluences. Furthermore, the structure depths fabricated under various laser parameters (Fig. 5E) were measured, and the corresponding profiles are shown in Figure S7.

The results indicate that as the incident laser fluence increases from $F = 0.099$ to 0.147 J cm^{-2} (Figure S6G-L), the regular distribution of LIPSSs is gradually deepened but keeping almost the same period. When the energy fluence becomes as low as $F = 0.099$ J cm^{-2}, the laser intensity is not strong enough to induce the amorphous phase transition, and the modulation depth of the LFE-LIPSSs shows hardly any change compared with the pre-LIPSSs (Fig. 5A). When the incident laser fluence increases, the electric field intensity inside the grooves will start to induce the locally selective amorphization. As shown in Figure S7K, the LFE-LIPSSs, bottleneck-like structures, appears to have a larger depth than the pre-LIPSSs. Furthermore, with increasing the laser fluence, an increased area of grooves will transform into the amorphous phase, and the structures gradually deepen (Figure S7G-J). When the laser fluence increases to $F = 0.147$ J cm^{-2} (Fig. 5B and Figure S7G), the spatial distribution of the LFE-LIPSSs is still highly homogenous with a modulation depth of 155 nm. However, as the energy fluence exceeds $F =$ 0.147 J cm^{-2}, the excessive energy gradually ablates the pre-LIPSSs with the generation of the disordered destructive structures and a decreased depth. In addition, as illustrated in Figure S6, the dotted arrays appear at the grooves, which could be ascribed to the electric field redistribution by existing LIPSSs and the incubation effect [45]. When the energy fluence increases to $F = 0.205$ J cm^{-2} (Fig. 5D), the depth of the ablated structures increases due to the destructive ablation by the excessive energy.

From the statistical results in Fig. 5E, we can conclude that the modulation depth of the LFE-LIPSSs fabricated by $F = 0.147$ J cm^{-2} reaches a maximum of about 155 nm, about three times larger than that of the pre-LIPSSs. It is worth noting that the optimal laser fluence ($F =$ 0.147 J cm^{-2}) is lower than that for fabricating the pre-LIPSSs ($F =$ 0.176 J cm^{-2}), which conclusively demonstrates the pre-LIPSSs could assist the light field enhancement localized within grooves. As a result, the proposed local field enhancement-assisted secondary spatial-

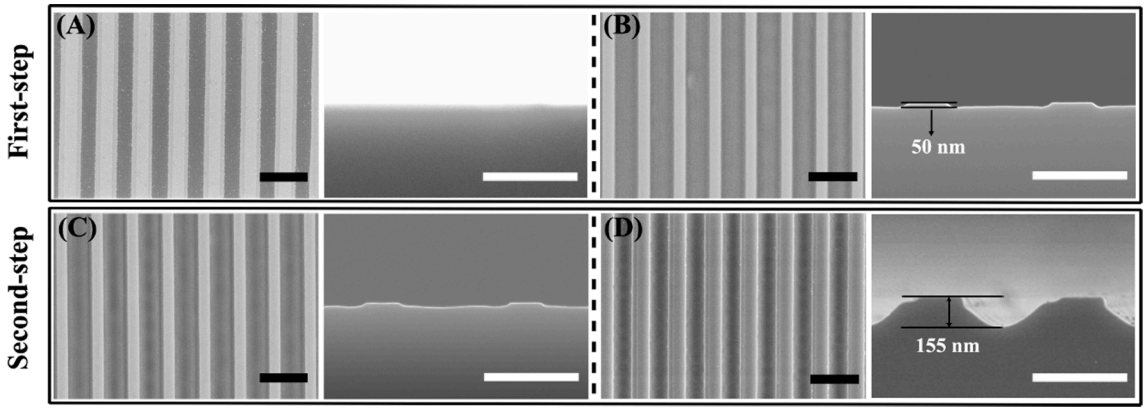

Fig. 3. SEM images of top-view (left) and cross-section view (right) of the LIPSSs fabricated by femtosecond laser irradiation and HF etching. In the first-step, the crystalline-amorphous LIPSSs were fabricated by femtosecond laser (A) and with HF etching (B). In the second-step, the LIPSSs were further processed by secondary amorphization (C) and chemical etching (D). The black scale bars are all 1 μm, and the white scale bars are all 0.5 μm.

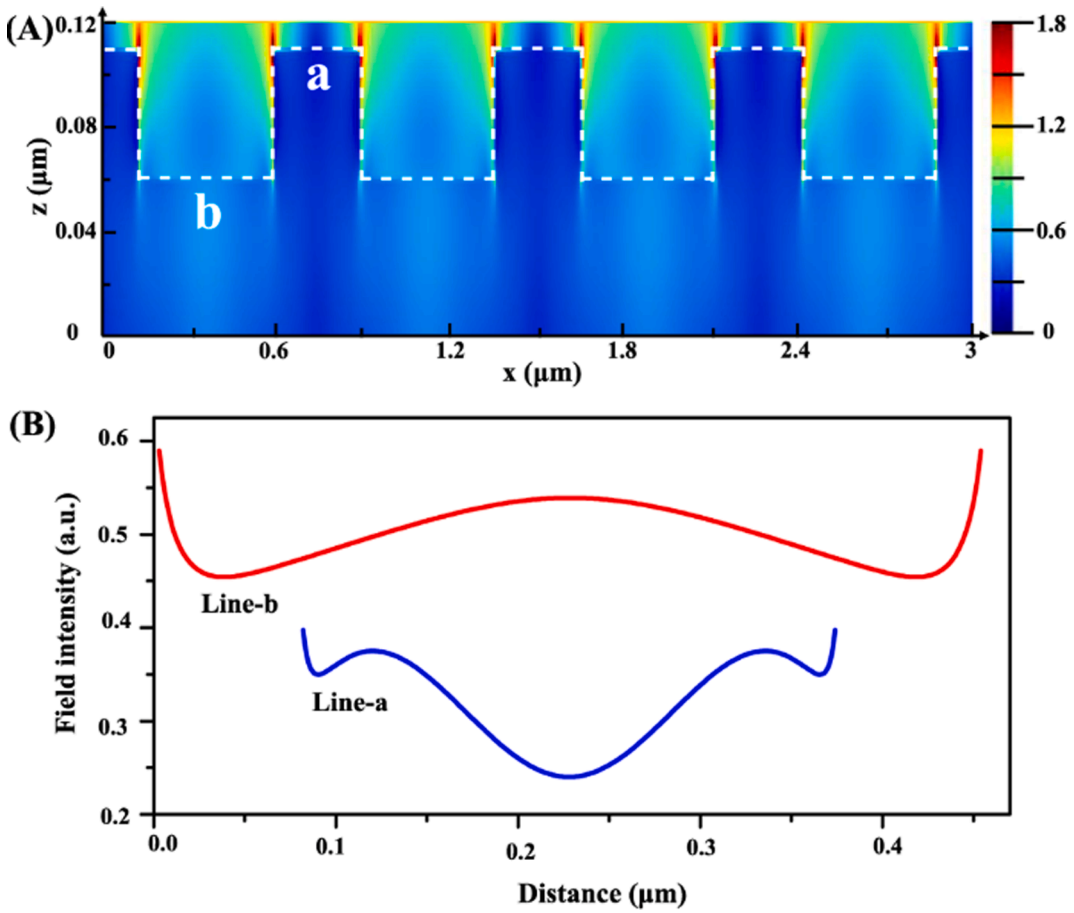

Fig. 4. (A) Simulated E-field intensity distribution for the LIPSSs in the x-z plane illuminated by 800 nm light. (B) The corresponding E-field intensity along the ripple and groove as marked in (A).

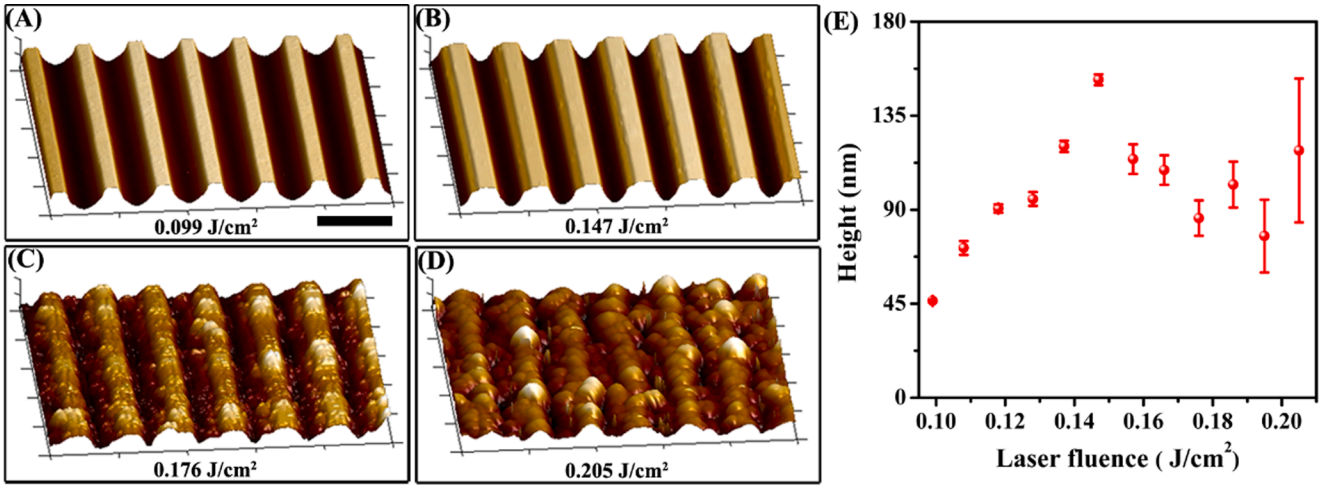

Fig. 5. Morphology dependence of the LFE-LIPSSs on femtosecond laser fluences. AFM images in (A-D) are the LFE-LIPSSs fabricated by different laser fluences at the fixed scanning velocity $v = 1$ mm s^{-1} with 40 min chemical etching. (E) Heights dependence of the LFE-LIPSSs on laser fluences. The scale bar is 1 μm.

selective amorphization strategy can fabricate deeper gratings and control the fabrication of gratings with different depths by varying the laser parameters and etching time. More importantly, the spatial period of the nanograting structures is constantly maintained during the deepening process. Various structures, including the bottleneck-like structures and the gratings with dotted arrays, can be fabricated for some special applications by tuning the femtosecond laser energy fluence.

In the previous work, Jiang et al. fabricated LIPSSs by femtosecond laser processing with KOH etching on silicon, [26] during which the obtained nanograting depth is in fact approximately 150 nm, similar to that of our LEF-LIPSSs. Even though the laser fabrication processes are similar, our technique essentially possesses the much difference and exhibits its own advantages. In this work, HF acid was employed instead

of KOH to remove the laser-treated amorphous Si regions rather than the crystalline regions, thus leaving the appearance of the crystalline Si nanogratings without any residual impurity, which is in fact more beneficial for applications in Si devices. Meanwhile, during the etching process, the crystalline Si flat surface is almost entirely retained, and the LFE-LIPSSs are developed underneath the Si surface. In addition, the currently proposed two-step spatial-selective amorphization strategy is of importance for femtosecond laser manufacturing, which focuses on taking advantage of structures to modulate the light field distribution on the surface in the second step.

3.3. Enhanced antireflection and polarization sensitivity of deep LFE-LIPSSs

The optical properties of materials can be effectively optimized or improved by controlling the feature size and shape of the surface nanostructures. Herein, we compared the optical properties among the flat Si, the shallow pre-LIPSSs, and the deep LFE-LIPSSs by the reflection spectral measurement. As shown in Figure S8A, the deep LFE-LIPSSs can exhibit the obviously enhanced antireflection within a wavelength range from λ = 400 nm to 1000 nm at normal incidence. As previously reported, the influence of the grating on the light reflection relies on the relationship between the incident light wavelength and grating period. In our case, the spatial period of the LIPSSs is $\Lambda = 765$ nm, being located within the measured wavelength range of $\lambda = 400$–1000 nm. Analysis of the antireflection spectrum of the grating structures identifies the following three points. First, for the period of $\Lambda < \lambda$, the subwavelength grating structures can contribute to achieve the gradual changes in the refractive index to result in the enhanced light trapping [46,47]. For the period of $\Lambda > \lambda$, in the alleged geometrical optics region, the absorptivity can be enhanced due to the light trapping effect of the LIPSSs [48]. When $\Lambda \approx \lambda$ in the strong diffraction region, the reflection of the LIPSSs would be significantly decreased [49]. Thus, the weak reflective region (corresponding to $\lambda = 650$–800 nm) of our results in Figure S8A may be ascribed to the strong diffraction of the gratings. In addition, both the modulation depth and surface roughness of the grating structures play significant roles in affecting the antireflection. As demonstrated in Fig. 5E and Figure S8AB, the statistical intensity of the reflection at around $\lambda \approx 700$ nm for different regular LIPSSs surfaces would like to decrease with increasing the depth. However, for the excessive laser fluence ($F = 0.205$ J cm^{-2}) irradiating on Si, the disordered rough surface can trap more lights to result in the lowest reflectivity. As shown in Fig. 6A, comparing with the pre-LIPSSs, the deep regular LFE-LIPSSs (obtained at $F = 0.147$ J cm^{-2}) exhibit 45% increase in antireflection performance at around $\lambda \approx 700$ nm.

Hence, the antireflection property of the Si surface nanostructures can be highly improved based on the two-step spatial-selective amorphization strategy, which is beneficial for the local field enhancement and the enhanced optical analysis. Based on this idea, we explore the SERS performance of such deep LFE-LIPSSs with a deposition of 20 nm thick Au film on the surface. Fig. 6B shows a comparison of the measured reflective spectra among three different silicon surfaces coated with Au films: the flat-Au, the shallow pre-LIPSSs-Au and the deep LFE-LIPSSs-Au. It is clearly that the deep LFE-LIPSSs-Au surface exhibits 47.8% and 43.5% increase in antireflection property at the wavelength around $\lambda = 700$ nm, compared with the flat-Au and the pre-LIPSSs-Au samples, respectively.

Therefore, the SERS activity of the deep LFE-LIPSSs was evaluated under the excitation of λ = 785 nm laser with 4-MBA as the probe molecules. Fig. 6C shows the measured SERS spectra on the surfaces of deep LFE-LIPSSs-Au, shallow pre-LIPSSs-Au, and flat-Au samples. The SERS spectrum of 4-MBA is dominated by the strong bands at approximately 1075 and 1588 cm^{-1}, assigning to υ_{12} (a_1) and υ_{8a} (a_1) aromatic ring characteristic vibrations. For the case of deep LFE-LIPSSs, the measured SERS spectra of 4-MBA molecules is not only much stronger than those on other two surface, but also appear more peaks at 1141 (υ_{15}, b_2) and 1180 (υ_9, a_1) cm^{-1} corresponding to C-H deformation modes, and at 1421 cm^{-1} corresponding to COO^--stretching vibration [50,51]. This is because, compared with the shallow pre-LIPSSs and the flat Si surfaces, both the depth and surface roughness of the deep LFE-LIPSSs are increased, which are favorable for localizing more light energy on the surface to generate the stronger E-field [52].

As discussed above, the geometric features of the LFE-LIPSSs such as the depth, the morphology and the arrangement regularity can be affected by tuning the laser fluences, which further influence the light field distribution on the surface. Thus, we investigated the effects of the structure morphology on the SERS properties. As shown in Figure S8C, with increasing the femtosecond laser energy fluences, the SERS performance of the structures shows the same varying trend as the height and antireflection characteristics. For the regular LFE-LIPSSs fabricated by the low laser fluence (from $F = 0.099$ to 0.147 J cm^{-2}), the SERS intensity increases with larger modulation height of the structures. When the laser fluence is higher than $F = 0.147$ J cm^{-2}, the detected Raman signals are significantly varied, which indicates an inhomogeneous distribution of the electromagnetic fields caused by the irregular LIPSSs. Eventhough the average SERS signal intensity is stronger, the poorly repeatable signal is inaccurate for practical analytical detection. As a result, by considering the enhanced capability and repeatability of SERS measurement, the LFE-LIPSSs fabricated under the laser fluence of $F = 0.147$ J cm^{-2} become the optimal. Thus, the overall variation trend of the SERS activity is the same as the antireflection property of the substrates.

The polarization response is another important characteristic of the grating structures. The corresponding reflective spectra under the light illumination with the polarization angles (θ) ranging from 0 to 180° relative to the grating direction are illustrated in Fig. 7A-C. The results indicate that the shallow pre-LIPSSs exhibit an obvious polarization dependent reflectivity response while the deep LFE-LIPSSs show an improved polarization dependent performance due to the enhanced light trapping behaviors. The reflectivity variation of the pre-LIPSSs is

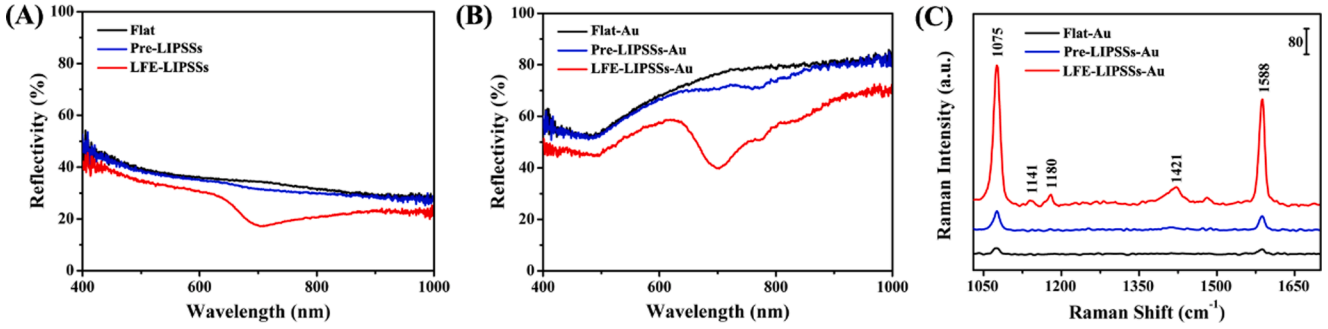

Fig. 6. The reflectivity and SERS intensity comparison of flat, pre-LIPSSs, and LFE-LIPSSs. (A) The reflectivity of Si flat, pre-LIPSSs, and LFE-LIPSSs. (B) The reflectivity and (C) SERS intensity of flat, pre-LIPSSs, and LFE-LIPSSs Si surface with 20 nm Au.

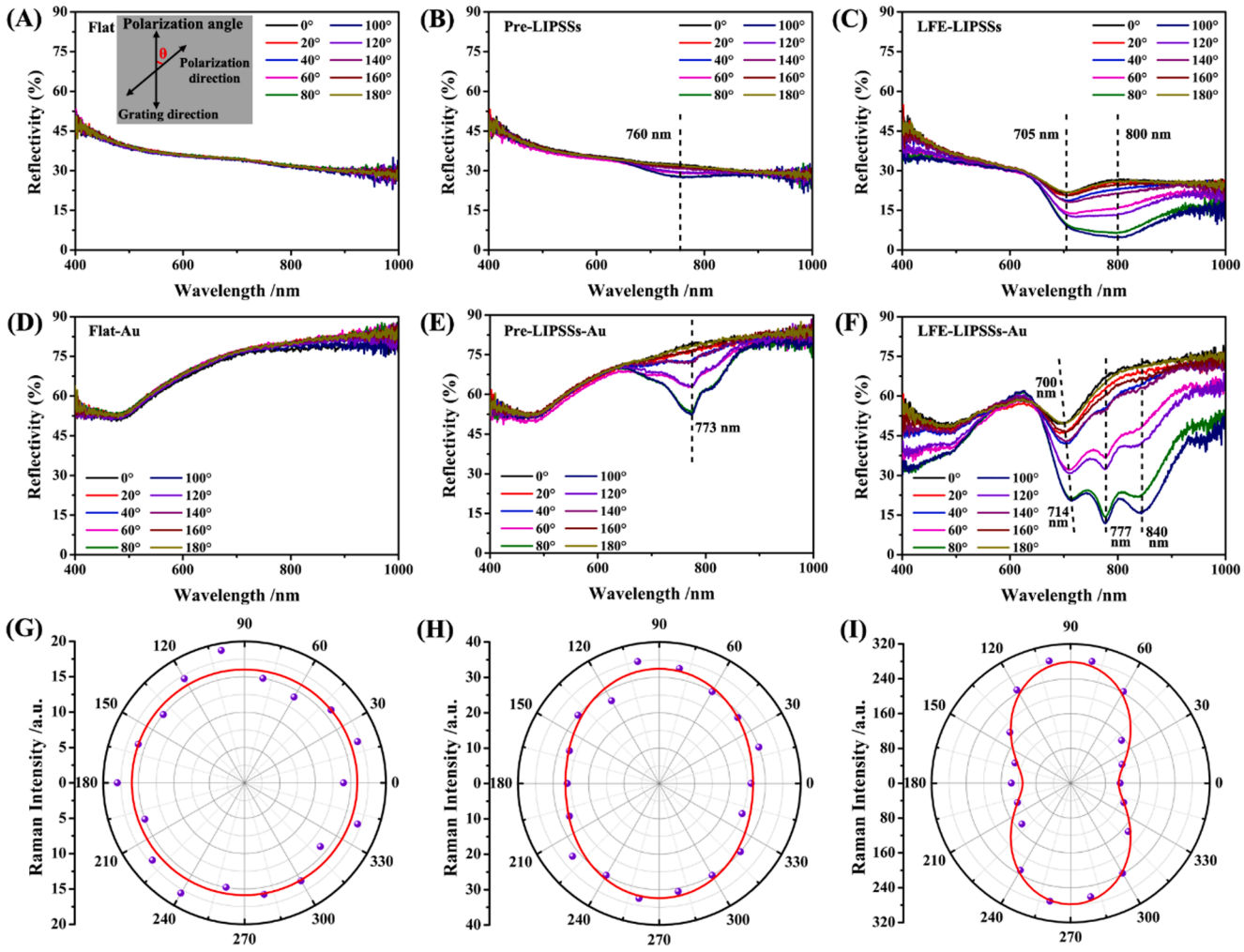

Fig. 7. Comparison of the polarization property in reflectivity (A-C) of flat, pre-LIPSSs and LFE-LIPSSs. The comparison of polarization in reflectivity (D-F) and SERS performance (G-I) of flat, pre-LIPSSs and LFE-LIPSSs surface with 20 nm Au. The insert schematic shows the polarization angle θ.

about 4.8% (from 32.2% to 27.4%) with different polarization angles at the wavelength of $\lambda = 760$ nm, as exhibited in Fig. 7B. Furthermore, in comparison with the shallow pre-LIPSSs, the reflectivity of the LFE LIPSSs is significantly reduced at $\lambda = 705$ nm (21.7%), when the light polarization is parallel with the LIPSSs orientation. As the polarization direction changes from parallel to perpendicular with the LIPSSs orientation, the reflectivity is reduced to 4.7%, and the antireflection peak gradually shifts to $\lambda = 800$ nm. After the deposition of 20 nm thick Au film on the structure surface, the polarization dependent response displays the same tendency as the above mentioned results, while there is a significant enhanced antireflection peak around the wavelength of $\lambda = 773$ nm for the pre-LIPSSs, and three antireflection peaks at the wavelength of $\lambda = 714$ nm, 777 nm, and 840 nm for the deep LFE-LIPSSs, which is caused by the surface plasmon resonance absorption of Au film. The variation of reflectivity for the shallow pre-LIPSSs is 26.6% at $\lambda = 773$ nm. However, for the deep LFE-LIPSSs, when the light polarization changes from parallel to perpendicular with the grating direction, the antireflection peak shifts from $\lambda = 714$ nm to 720 nm, and two new peaks appear at $\lambda = 777$ nm and 840 nm. The measured variations of reflectivity are 29.1% (from $\lambda = 700$ nm to 714 nm), 54.9% ($\lambda = 777$ nm), and 55.1% ($\lambda = 840$ nm), respectively. The enhanced antireflective property of the deep LFE-LIPSSs shows a great potential for applications in near infrared detection.

In addition, SERS properties of the surfaces excited by the polarized light at the wavelength of $\lambda = 785$ nm are further studied under various polarization angles of θ. The corresponding polarization dependent SERS performances for the flat, pre-LIPSSs and LFE-LIPSSs are shown in Figure S9. Fig. 7G-I display the change of SERS intensities for each substrate with varying θ angles at the 1588 cm^{-1} band. The results indicate that the deep LFE-LIPSSs based substrate has a stronger polarization dependent response than the shallow pre-LIPSSs, while the flat surface has no apparent change. While varying the polarization angles, the SERS intensity exhibits the weakest when the polarization direction is parallel to the LIPSSs ($\theta = 0°$). As the polarization angle increases, the SERS intensity gradually increases and becomes strongest at $\theta = 90°$, where the polarization is perpendicular to LIPSSs orientation. The experimental results from different polarization angles can be fitted to the related $\sin^2$ curve, consistent with the previous reports:[53].

$$EF \approx \left|\frac{E_{max}}{E_0}\right|^4 sin^2(\theta) \quad (1)$$

Furthermore, the anisotropy ratios for the shallow pre-LIPSSs and deep LFE-LIPSSs can be calculated by the following equation:[54].

$$\sigma = \frac{I_{max} - I_{min}}{I_{max} + I_{min}} \quad (2)$$

where I_{max} and I_{min} are the measured SERS intensities at the polarization angle $\theta = 90°$ and 0°, respectively. Therefore, the anisotropy ratios (σ) for the pre-LIPSSs and LFE-LIPSSs approximate 0.11 and 0.43, respectively, which indicates a more sensitive polarization-dependence of the deep LFE-LIPSSs. These results are consistent with the reflectivity for the two structures with the deposition of 20 nm Au film. According to

Equation (1), the polarization-dependence enhanced factor is proportional to the enhanced electric field and $\sin^2\theta$. When the θ is given, the SERS intensity of LIPSSs depends on the electric field, so the SERS intensity of the deep LFE-LIPSSs will be larger due to the stronger localized surface plasmon resonance (LSPR) effect. As the polarization angle varies from $\theta = 0^\circ$ to 90°, the SERS intensities of LFE-LIPSSs increase significantly greater than that of pre-LIPSSs. As a result, according to Equation (2), the deep LFE-LIPSSs will have a larger anisotropy ratio, and exhibit the superior SERS polarization dependence performance.

To further evaluate the effect of the structure on the polarization response property with different excitation wavelengths, we deposited 20 nm thick Ag film instead of Au film on the deep LFE-LIPSSs due to the long-range SERS performance of the former material. Taking into account the common laser wavelengths in Raman detection, three wavelengths, $\lambda = 473$ nm, 532 nm and 785 nm, are selected for SERS testing based on the deep LFE-LIPSSs with 20 nm thick Ag coating. Using 4-MBA as probe molecules, the measured SERS spectra are shown in Figure S10, and the statistical results measured by three lights are displayed in Fig. 8A-C. And their calculated anisotropy ratios (σ) are 0.33 ($\lambda = 473$ nm), 0.12 ($\lambda = 532$ nm), and 0.73 ($\lambda = 785$ nm), respectively. The results indicate that the deep LFE-LIPSSs-Ag sample exhibits the strongest SERS polarization dependence effect under $\lambda = 785$ nm light excitation, while that under $\lambda = 532$ nm light excitation is the weakest. As previously reported, the LSPR property of the surface nanostructures is directly related to the surface adsorption properties, which can be expressed by the reflection property [55]. Thus, to better explore the polarization SERS performance under different light excitations, the reflection spectra of the deep LFE-LIPSSs-Ag surface were further examined. Fig. 8D shows the reflection spectra for the deep LFE-LIPSSs-Ag sample under different incident light polarizations, while Fig. 8E exhibits the spectra intensity distributions. The polarization angle dependent spectra intensities at the excitation wavelengths of $\lambda = 473$ nm, 532 nm, and 785 nm are plotted in Fig. 8F, which indicates the LFE-LIPSSs exhibit a strongest polarization dependence effect under $\lambda = 785$ nm irradiation and the weakest one at $\lambda = 532$ nm. It means that the light field localization ability of the deep LFE-LIPSSs-Ag sample to different light wavelengths is as follows: 785 nm > 473 nm > 532 nm, which is consistent with the tendency of the polarization dependence effect in the SERS measurement under different excitation lasers. In addition, the FDTD simulation of E-field for the three excitation lights with different polarization directions are exhibited in Fig. 8G-I, and the simulated E-field polarization dependence tendencies are similar to practical SERS experimental results. It is found from the simulation results when the incident light polarization is parallel to the grating direction, the intensity of E-field is similar for various light wavelengths. As the incident light polarization is perpendicular to the grating direction, the intensity of E-field becomes significantly varied for different light wavelengths, and the deep LFE-LIPSSs can exhibit the strong SERS polarization

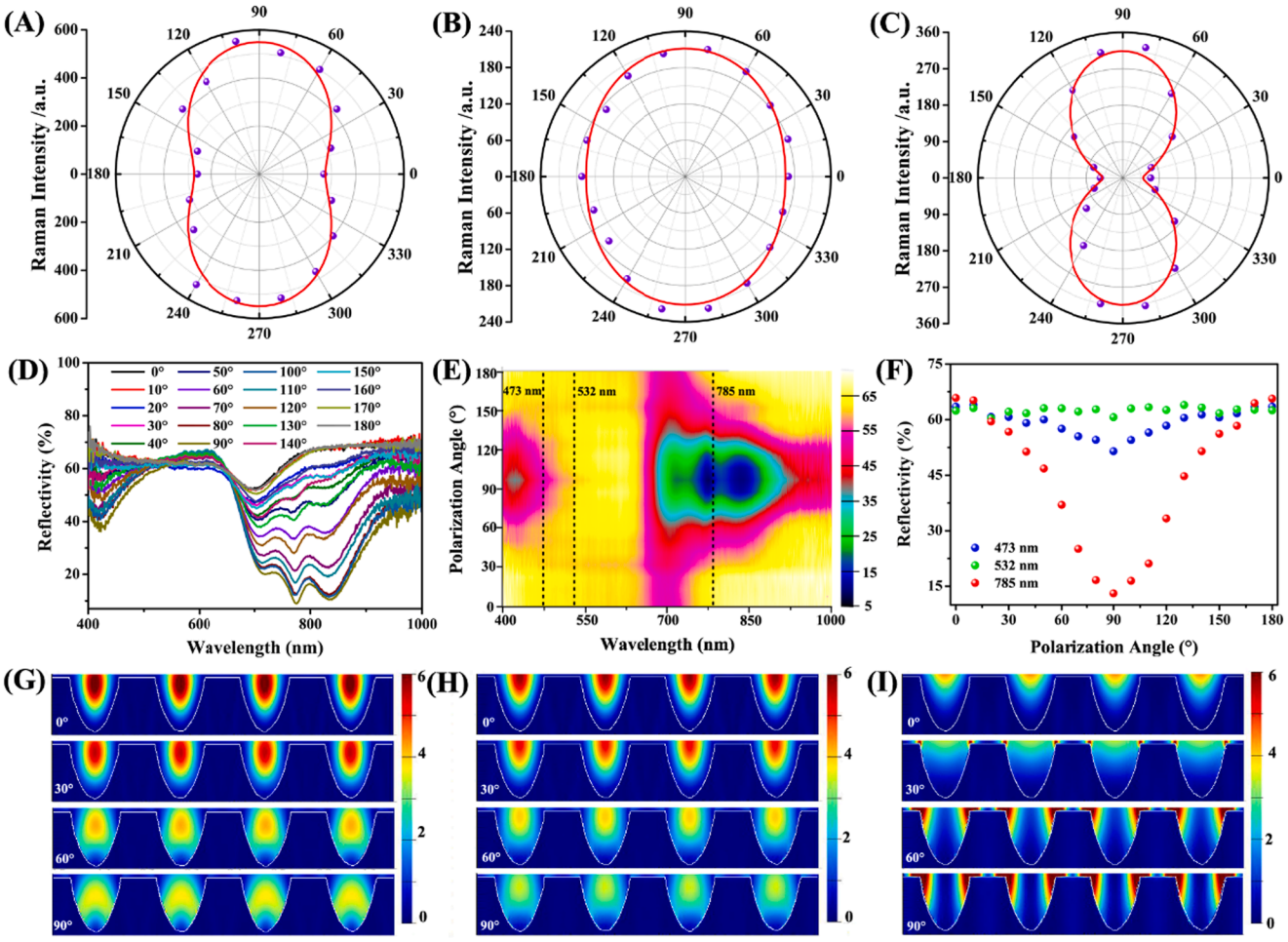

Fig. 8. (A-C) The experimental SERS polarization dependence results of LFE-LIPSSs with 20 nm Ag at 1588 cm^{-1} band excited by the different laser wavelengths, $\lambda =$ 473 nm, 532 nm, and 785 nm, respectively. The red lines are fitted curves of the $\sin^2$ function. The reflection spectra (D) and intensity (E) for LFE-LIPSSs under different polarization incident light ($\lambda = 400$–1000 nm). The scale bar on the right represents the intensity of reflectivity. Furthermore, the reflectivity of $\lambda = 473$ nm, 532 nm, and 785 nm under different polarization angles are displayed in (F). Spatial E-field distribution of LFE-LIPSSs with 20 nm Ag in the x-z plane with various polarization angles under (G) $\lambda = 473$ nm, (H) $\lambda = 532$ nm, (I) $\lambda = 785$ nm, respectively.

dependence under the excitation wavelength of $\lambda = 785$ nm.

4. Conclusions

In summary, a large area uniform deep LIPSSs are successfully fabricated by the proposed two-step spatial-selective amorphization approach, which can effectively enhance the antireflection and polarization properties of the Si surface. Our novel method of processing LFE-LIPSSs successfully fabricates deeper and regular LIPSSs, which provides a new insight for femtosecond laser-based nanofabrication. In the first amorphous step, the uniform crystalline-amorphous gratings are created on surface due to the interaction of weak SPP and incident laser, and the shallow pre-LIPSSs (50 nm) are obtained by the following HF etching with a period of 765 nm. During the second-step process, the intensity distribution of incident energy is modulated by pre-LIPSSs, with local field enhancement in the grooves for further spatial-selective amorphization. After chemical etching over again, the acquired regular LFE-LIPSSs (155 nm) depth is three times than that of the pre-LIPSSs, with an invariable period. Compared with the pre-LIPSSs, the Si nanograting structures fabricated based on the LFE-LIPSSs strategy exhibit 45% increase in antireflection performance at around 700 nm. The corresponding SERS anisotropy ratio (σ) of LFE-LIPSSs (0.43) is improved by about four times compared to that of the pre-LIPSSs (0.11). The LFE-LIPSSs strategy can not only be applied to enhance the antireflection and SERS polarization dependence performance of nanostructures, but also benefit for designing photoelectric detectors, nanofluidics and optical communication devices. In addition, the proposed method provides a new approach for femtosecond laser fabrication that can likely be applied to other materials.

Funding.

This work was supported by the Natural Science Foundation of China (NSFC, Grant Nos. 91750205, 61705227); Jilin Provincial Science & Technology Development Project (Grant No. 20200201086JC); “Shu Guang” Talent Program of Chang Chun Institute of Optics, Fine Mechanics and Physics; K. C. Wong Education Foundation (GJTD-2018–08); Open Project of State Key Laboratory of Supramolecular Structure and Materials (Grant No. sklssm2021024); Opening Project of the Key Laboratory of Bionic Engineering (Ministry of Education), Jilin University, K201905.

CRediT authorship contribution statement

Xiuyun Li: Conceptualization, Methodology, Writing – original draft. **Ruiyan Li:** Resources, Data curation. **Zhi Yu:** Conceptualization, Writing – review & editing, Funding acquisition. **Jun Xing:** Validation. **Wenchi Kong:** Resources. **Yue Wang:** Funding acquisition. **Jianjun Yang:** Writing – review & editing, Funding acquisition.

Declaration of Competing Interest

The authors declare that they have no known competing financial interests or personal relationships that could have appeared to influence the work reported in this paper.

Appendix A. Supplementary data

Supplementary data to this article can be found online at https://doi.org/10.1016/j.apsusc.2022.152965.

References

[1] T.-H. Her, R.J. Finlay, C. Wu, S. Deliwala, E. Mazur, Microstructuring of silicon with femtosecond laser pulses, Appl. Phys. Lett. 73 (1998) 1673–1675.
[2] A.Y. Vorobyev, C. Guo, Antireflection effect of femtosecond laser-induced periodic surface structures on silicon, Opt. Express 19 (S5) (2011) A1031, https://doi.org/10.1364/OE.19.0A1031.
[3] H. Lu, Z. Yue, Y. Li, Y. Zhang, M. Zhang, W. Zeng, X. Gan, D. Mao, F. Xiao, T. Mei, W. Zhao, X. Wang, M. Gu, J. Zhao, Magnetic plasmon resonances in nanostructured topological insulators for strongly enhanced light-MoS_2 interactions, Light: Sci. Appl. 9 (2020) 191.
[4] X. Zhu, W. Yan, Uriel Levy, N. Asger Mortensen, A. Kristensen, Resonant laser printing of structural colors on high-index dielectric metasurfaces, Sci. Adv. 3 (2017), e1602487.
[5] Y. Su, Y. Ke, S. Cai, Q. Yao, Surface plasmon resonance of layer-by-layer gold nanoparticles induced photoelectric current in environmentally-friendly plasmon-sensitized solar cell, Light: Sci. Appl. 1 (6) (2012) e14.
[6] S.A. Jalil, B. Lai, M. ElKabbash, J. Zhang, E.M. Garcell, S. Singh, C. Guo, Spectral absorption control of femtosecond laser-treated metals and application in solar-thermal devices, Light: Sci. Appl. 9 (2020) 14.
[7] B. Xu, L. Wang, Z. Ma, R. Zhang, Q. Chen, C. Lv, B. Han, X. Xiao, X. Zhang, Y. Zhang, K. Ueno, H. Misawa, H. Sun, Surface-Plasmon-Mediated Programmable Optical Nanofabrication of an Oriented Silver Nanoplate, ACS Nano 8 (7) (2014) 6682–6692.
[8] Y. Tian, H. Wang, L. Yan, X. Zhang, A. Falak, Y. Guo, P. Chen, F. Dong, L. Sun, W. Chu, A Generalized Methodology of Designing 3D SERS Probes with Superior Detection Limit and Uniformity by Maximizing Multiple Coupling Effects, Adv. Sci. 6 (2019) 1900177.
[9] P. Ran, L. Jiang, X. Li, B.o. Li, P. Zuo, Y. Lu, Femtosecond Photon-Mediated Plasma Enhances Photosynthesis of Plasmonic Nanostructures and Their SERS Applications, Small 15 (11) (2019) 1804899, https://doi.org/10.1002/smll.v15.1110.1002/smll.201804899.
[10] K. Ding, C.Z. Ning, Metallic subwavelength-cavity semiconductor nanolasers, Light: Sci. Appl. 1 (7) (2012) e20.
[11] C. Stelling, S. Fossati, J. Dostalek, M. Retsch, Surface plasmon modes of nanomesh-on-mirror nanocavities prepared by nanosphere lithography, Nanoscale 10 (37) (2018) 17983–17989.
[12] R. Chen, Y. Zhou, W. Chen, R. Chen, N. Iqbal, Y. Ma, Multifunctional Metasurface: Coplanar Embedded Design for Metalens and Nanoprinted Display, ACS Photon. 7 (5) (2020) 1171–1177.
[13] M.W. Klein, M. Wegener, N. Feth, S. Linden, Experiments on second- and third-harmonic generation from magnetic metamaterials, Opt. Express 15 (8) (2007) 5238, https://doi.org/10.1364/OE.15.005238.
[14] S. Daqiqeh Rezaei, J. Ho, T. Wang, S. Ramakrishna, J.K.W. Yang, Direct Color Printing with an Electron Beam, Nano Lett. 20 (6) (2020) 4422–4429.
[15] P. Shi, J. Zhang, H.-Y. Lin, P.W. Bohn, Effect of Molecular Adsorption on the Electrical Conductance of Single Au Nanowires Fabricated by Electron-Beam Lithography and Focused Ion Beam Etching, Small 6 (22) (2010) 2598–2603.
[16] X. Jia, L. Wang, N. Zhuo, J. Zhang, S. Zhai, J. Liu, S. Liu, F. Liu, Z. Wang, Multi-wavelength sampled Bragg grating quantum cascade laser arrays, Photon. Res. 6 (2018) 721.
[17] Z. Ma, Y. Zhang, B. Han, Q. Chen, H. Sun, Femtosecond-Laser Direct Writing of Metallic Micro/Nanostructures: From Fabrication Strategies to Future Applications, Small Methods 2 (2018) 1700413.
[18] O. Tokel, A. Turnalı, G. Makey, P. Elahi, T. Çolakoğlu, E. Ergeçen, Ö. Yavuz, R. Hübner, M. Zolfaghari Borra, I. Pavlov, A. Bek, R. Turan, D.K. Kesim, S. Tozburun, S. Ilday, F.Ö. Ilday, In-chip microstructures and photonic devices fabricated by nonlinear laser lithography deep inside silicon, Nat. Photon. 11 (2017) 639–645.
[19] K.C. Phillips, H.H. Gandhi, E. Mazur, S.K. Sundaram, Ultrafast laser processing of materials: a review, Adv. Opt. Photon. 7 (4) (2015) 684, https://doi.org/10.1364/AOP.7.000684.
[20] M. Birnbaum, Semiconductor Surface Damage Produced by Ruby Lasers, J. Appl. Phys. 36 (1965) 3688–3689.
[21] C. Lopez-Santos, D. Puerto, J. Siegel, M. Macias-Montero, C. Florian, J. Gil-Rostra, V. López-Flores, A. Borras, A.R. González-Elipe, J. Solis, Anisotropic Resistivity Surfaces Produced in ITO Films by Laser-Induced Nanoscale Self-organization, Adv. Opt. Mater. 9 (2020) 2001086.
[22] X. Zheng, C. Cong, Y. Lei, J. Yang, C. Guo, Formation of Slantwise Surface Ripples by Femtosecond Laser Irradiation, Nanomaterials (Basel) 8 (2018) 458.
[23] S.A. Jalil, J. Yang, M. ElKabbash, S.C. Singh, C. Guo, Maskless formation of uniform subwavelength periodic surface structures by double temporally-delayed femtosecond laser beams, Appl. Surf. Sci. 471 (2019) 516–520.
[24] L. Wang, Q.D. Chen, X.W. Cao, R. Buividas, X. Wang, S. Juodkazis, H.B. Sun, Plasmonic nano-printing: large-area nanoscale energy deposition for efficient surface texturing, Light: Sci. Appl. 6(2017) e17112.
[25] X. Li, G. Yuan, W. Yu, J. Xing, Y. Zou, C. Zhao, W. Kong, Z. Yu, C. Guo, A self-driven microfluidic surface-enhanced Raman scattering device for Hg^{2+} detection fabricated by femtosecond laser, Lab Chip 20 (2020) 414–423.
[26] J. Huang, L. Jiang, X. Li, A. Wang, Z. Wang, Q. Wang, J. Hu, L. Qu, T. Cui, Y. Lu, Fabrication of highly homogeneous and controllable nanogratings on silicon via chemical etching-assisted femtosecond laser modification, Nanophotonics-Berlin 8 (2019) 869–878.
[27] S. Xu, C. Yao, H. Dou, W. Liao, X. Li, R. Ding, L. Zhang, H. Liu, X. Yuan, X. Zu, An investigation on 800 nm femtosecond laser ablation of K9 glass in air and vacuum, Appl. Surf. Sci. 406 (2017) 91–98.
[28] S. Xu, K. Sun, C. Yao, H. Liu, X. Miao, Y. Jiang, H. Wang, X. Jiang, X. Yuan, X. Zu, Periodic surface structures on dielectrics upon femtosecond laser pulses irradiation, Opt. Express 27 (6) (2019) 8983, https://doi.org/10.1364/OE.27.008983.
[29] S. Gräf, C. Kunz, F. Müller, Formation and Properties of Laser-Induced Periodic Surface Structures on Different Glasses, Materials 10 (8) (2017) 933, https://doi.org/10.3390/ma10080933.

[30] H. Qiao, J. Yang, F. Wang, Y. Yang, J. Sun, Femtosecond laser direct writing of large-area two-dimensional metallic photonic crystal structures on tungsten surfaces, Opt. Express 23 (20) (2015) 26617, https://doi.org/10.1364/OE.23.026617.
[31] S. Bai, D. Serien, A. Hu, K. Sugioka, 3D Microfluidic Surface-Enhanced Raman Spectroscopy (SERS) Chips Fabricated by All-Femtosecond-Laser-Processing for Real-Time Sensing of Toxic Substances, Adv. Funct. Mater. 28 (2018) 1706262.
[32] T. Zou, B. Zhao, W. Xin, Y. Wang, B. Wang, X. Zheng, H. Xie, Z. Zhang, J. Yang, C. L. Guo, High-speed femtosecond laser plasmonic lithography and reduction of graphene oxide for anisotropic photoresponse, Light Sci. Appl. 9 (2020) 69.
[33] Y. Zhang, Q. Jiang, K. Cao, T. Chen, K. Cheng, S. Zhang, D. Feng, T. Jia, Z. Sun, J. Qiu, Extremely regular periodic surface structures in a large area efficiently induced on silicon by temporally shaped femtosecond laser, Photon. Res. 9 (2021) 839.
[34] D. Puerto, M. Garcia-Lechuga, J. Hernandez-Rueda, A. Garcia-Leis, S. Sanchez-Cortes, J. Solis, J. Siegel, Femtosecond laser-controlled self-assembly of amorphous-crystalline nanogratings in silicon, Nanotechnology 27 (2016), 265602.
[35] M. Garcia-Lechuga, D. Puerto, Y. Fuentes-Edfuf, J. Solis, J. Siegel, Ultrafast Moving-Spot Microscopy: Birth and Growth of Laser-Induced Periodic Surface Structures, ACS Photon. 3 (2016) 1961–1967.
[36] Y. Fuentes-Edfuf, M. Garcia-Lechuga, D. Puerto, C. Florian, A. Garcia-Leis, S. Sanchez-Cortes, J. Solis, J. Siegel, Coherent scatter-controlled phase-change grating structures in silicon using femtosecond laser pulses, Sci. Rep. 7 (2017) 4594.
[37] J. Huang, L. Jiang, X. Li, Q. Wei, Z. Wang, B. Li, L. Huang, A. Wang, Z. Wang, M. Li, L. Qu, Y. Lu, Cylindrically Focused Nonablative Femtosecond Laser Processing of Long-Range Uniform Periodic Surface Structures with Tunable Diffraction Efficiency, Adv. Opt. Mater. 7 (2019) 1900706.
[38] K. Cao, L. Chen, H. Wu, J. Liu, K. Cheng, Y. Li, Y. Xia, C. Feng, S. Zhang, D. Feng, Z. Sun, T. Jia, Large-area commercial-grating-quality subwavelength periodic ripples on silicon efficiently fabricated by gentle ablation with femtosecond laser interference via two cylindrical lenses, Opt. Laser Technol. 131 (2020), 106441.
[39] M. Huang, F. Zhao, Y. Cheng, N. Xu, Z. Xu, Origin of laser-induced near-subwavelength ripples: interference between surface plasmons and incident laser, Acs Nano 3 (2009) 4062–4070.
[40] W. Cao, L. Jiang, J. Hu, A. Wang, X. Li, Y. Lu, Optical Field Enhancement in Au Nanoparticle-Decorated Nanorod Arrays Prepared by Femtosecond Laser and Their Tunable Surface-Enhanced Raman Scattering Applications, ACS Appl Mater Interfaces 10 (2018) 1297–1305.
[41] T.-Y. Derrien, J. Krüger, T.E. Itina, S. Höhm, A. Rosenfeld, J. Bonse, Rippled area formed by surface plasmon polaritons upon femtosecond laser double-pulse irradiation of silicon, Opt. Express 21 (24) (2013) 29643, https://doi.org/10.1364/OE.21.029643.
[42] X. Liu, B. Bai, Q. Chen, H. Sun, Etching-assisted femtosecond laser modification of hard materials, Opto-Electron. Adv. 2 (9) (2019) 19002101–19002114.
[43] Y. Hu, S. Rao, S. Wu, P. Wei, W. Qiu, D. Wu, B. Xu, J. Ni, L. Yang, J. Li, J. Chu, K. Sugioka, All-Glass 3D Optofluidic Microchip with Built-in Tunable Microlens Fabricated by Femtosecond Laser-Assisted Etching, Adv. Opt. Mater. 6 (9) (2018) 1701299, https://doi.org/10.1002/adom.v6.910.1002/adom.201701299.
[44] X. Yu, Q. Zhang, D. Qi, S. Tang, S. Dai, P. Zhang, Y. Xu, X. Shen, Femtosecond laser-induced large area of periodic structures on chalcogenide glass via twice laser direct-writing scanning process, Opt. Laser Technol. 124 (2020) 105977, https://doi.org/10.1016/j.optlastec.2019.105977.
[45] X.u. Ji, L. Jiang, X. Li, W. Han, Y. Liu, A. Wang, Y. Lu, Femtosecond laser-induced cross-periodic structures on a crystalline silicon surface under low pulse number irradiation, Appl. Surf. Sci. 326 (2015) 216–221.
[46] D.H. Raguin, G.M. Morris, Analysis of antireflection-structured surfaces with continuous one-dimensional surface profiles, Appl. Opt. 32 (1993) 2582–2598.
[47] N. Das, D. Chandrasekar, M. Nur-E-Alam, M.M.K. Khan, Light Reflection Loss Reduction by Nano-Structured Gratings for Highly Efficient Next-Generation GaAs Solar Cells, Energies 13 (2020) 4198.
[48] F. Ghmari, T. Ghbara, M. Laroche, R. Carminati, J.-J. Greffet, Influence of microroughness on emissivity, J. Appl. Phys. 96 (2004) 2656–2664.
[49] S. Hava, M. Auslender, D. Rabinovich, Operator approach to electromagnetic coupled-wave calculations of lamellar gratings: infrared optical properties of intrinsic silicon gratings, Appl. Opt. 33 (1994) 4807–4813.
[50] L. Yang, X. Jiang, W. Ruan, J. Yang, B. Zhao, W. Xu, J.R. Lombardi, Charge-transfer-induced surface-enhanced Raman scattering on Ag-TiO_2 nanocomposites, J. Phys. Chem. C 113 (2009) 16226–16231.
[51] X. Jiang, D.i. Yin, M. Yang, J. Du, W. Wang, L. Zhang, L. Yang, X. Han, B. Zhao, Revealing interfacial charge transfer in TiO_2/reduced graphene oxide nanocomposite by surface-enhanced Raman scattering (SERS): Simultaneous a superior SERS-active substrate, Appl. Surf. Sci. 487 (2019) 938–944.
[52] Z. Li, Mesoscopic and Microscopic Strategies for Engineering Plasmon-Enhanced Raman Scattering, Adv. Opt. Mater. 6 (16) (2018) 1701097, https://doi.org/10.1002/adom.v6.1610.1002/adom.201701097.
[53] H. Wei, F. Hao, Y. Huang, W. Wang, P. Nordlander, H. Xu, Peter Nordlander, and Hongxing Xu, Polarization Dependence of Surface-Enhanced Raman Scattering in Gold Nanoparticle-Nanowire Systems, Nano Lett. 8 (8) (2008) 2497–2502.
[54] W. Xin, X. Li, X. He, B. Su, X. Jiang, K. Huang, X. Zhou, Z. Liu, J. Tian, Black-Phosphorus-Based Orientation-Induced Diodes, Adv. Mater. 30 (2) (2018) 1704653, https://doi.org/10.1002/adma.v30.210.1002/adma.201704653.
[55] A. Toma, D. Chiappe, C. Boragno, F. Buatier de Mongeot, Self-organized ion-beam synthesis of nanowires with broadband plasmonic functionality, Phys. Rev. B 81 (16) (2010), https://doi.org/10.1103/PhysRevB.81.165436.